Available online at www.sciencedirect.com
ScienceDirect
Comput. Methods Appl. Mech. Engrg. 329 (2018) 532–552
Computer methods in applied mechanics and engineering
www.elsevier.com/locate/cma

An Eulerian–Lagrangian incompressible SPH formulation (ELI-SPH) connected with a sharp interface

G. Fourtakas*, P.K. Stansby, B.D. Rogers, S.J. Lind

School of Mechanical, Aerospace and Civil Engineering, The University of Manchester, Manchester, M13 9PL, UK

Received 13 February 2017; received in revised form 1 June 2017; accepted 22 September 2017
Available online 20 October 2017

Highlights

- An Eulerian–Lagrangian incompressible SPH (ELI-SPH) formulation with a single interface has been developed.
- A simple Eulerian solid boundary condition within an otherwise Lagrangian framework has been demonstrated.
- ELI-SPH is demonstrated for internal and free-surface flows with convergence.
- Improved accuracy results from the particle uniformity of the Eulerian region.
- Pressure and velocity fields remain noise-free.

Abstract

An Eulerian–Lagrangian incompressible SPH (ELI-SPH) formulation is proposed that improves accuracy over a fully Lagrangian formulation for many problems. This develops the original formulation of Lind and Stansby (2016) by providing a sharp interface rather than a transition zone. This is generally convenient and avoids any need for Arbitrary Lagrangian Eulerian (ALE) particle mass correction. It also enables a simple, accurate solid boundary condition in a Lagrangian formulation by having the interface close to the solid boundary with an Eulerian fluid domain typically three particles thick with mirror particles. Particle regularisation is necessary in a Lagrangian domain and we apply a general form based on Fick's shifting which is modified at the interface by ignoring Eulerian particles and using mirror particles to give zero concentration gradient and hence zero shifting across the interface, avoiding spurious migration. Continuity is enforced at the interface as part of the combined Eulerian–Lagrangian domain. The formulation is validated against the analytical solution for Taylor–Green vortices, vortex spin down in a box, and propagating waves. The use of mixed kernel order in the Eulerian domain is also demonstrated.

Keywords: Incompressible SPH; Lagrangian SPH; Eulerian SPH; ALE; Eulerian solid boundary conditions; Improved accuracy

* Corresponding author.
E-mail address: georgios.fourtakas@manchester.ac.uk (G. Fourtakas).

https://doi.org/10.1016/j.cma.2017.09.029

1. Introduction

The incompressible smoothed particle hydrodynamics (ISPH) scheme satisfies continuity with a divergence-free velocity field using the projection method, as for mesh-based methods. ISPH is known to be accurate with near noise-free pressures and kinematics for internal and free-surface flows, following recent developments of the diffusion-based particle shifting algorithms for particle regularisation [1,2]. However some non-uniformity of particles persists compared to regular spacing, restricting the accuracy and consequently the convergence of solutions to lower than the theoretical maximum second-order convergence. Several techniques have been developed to improve the accuracy of the solution by using kernel corrections with first-order consistency [3] and/or re-meshing of the domain either using an iterative method or by re-initialisation of the particles to their original distribution [4] but re-meshing techniques tend to be costly and cumbersome.

The recent development of high-order incompressible SPH within an Eulerian framework [5] has removed the error associated with non-uniformity of particles, and demonstrated near ideal convergence characteristics defined by the order of the kernel with up to sixth order tested. However, free-surface or interfacial flows generally require the Lagrangian form of SPH. Combining the advantages of both Eulerian and Lagrangian incompressible SPH (ELI-SPH) creates a modelling framework for SPH that improves accuracy without restricting applications and a transition from Eulerian to Lagrangian form is thus necessary.

Lind and Stansby [5] demonstrated the use of a transition zone for this purpose in an Arbitrary Eulerian–Lagrangian (ALE) formulation with a smooth weighting for the advection term and applied this successfully to wave propagation. For many problems a sharp interface would however be convenient without the complication of an intermediate ALE region. The Eulerian and Lagrangian formulations would thus be unchanged but the interface requires particular modification of the shifting algorithm necessary in the Lagrangian domain to avoid spurious migration of particles from the Lagrangian to the Eulerian domain, while satisfying continuity through zero divergence. A method is presented in this paper based on mirror particles at the interface to define shifting and accuracy and convergence is demonstrated for canonical two-dimensional internal and wave flows.

With such a scheme the Lagrangian zone may be restricted to the proximity of a free surface or interface, which may be highly distorted, with high accuracy in the adjoining Eulerian zone. The Eulerian zone may contain regions with different order of kernels with high order regions further improving accuracy. This approach is also demonstrated.

Wholly Lagrangian formulations may still be preferred for certain flows, for example with multi-phase interactions, and the present approach provides a simple and accurate way of representing solid boundaries with full kernel support. This is achieved with a thin Eulerian layer in the flow with mirror particles and an interface close to the boundary. This is demonstrated here with a layer three particles in thickness. Such an approach applies equally to weakly compressible SPH.

Potential applications of the scheme are highly non-linear flows where the Lagrangian features of SPH are desirable near the vicinity of a material interface and a free-surface region, whereas the Eulerian formulation can be applied on the remaining domain. Another advantage is the framework it provides when coupling to other Eulerian schemes allowing for a fully Eulerian hybrid solver at the interface and removing the difficulties associated with coupling a moving Lagrangian zone. Extension to three dimensions is logical.

This paper is organised as follows; Section 2 describes briefly the SPH formalism and Section 3 the Lagrangian formulation and operators. Section 4 describes the Eulerian–Lagrangian (ELI-SPH) methodology with the interface approach. In Section 5 the results from canonical periodic and wall-bounded and wave propagation test cases are shown and discussed. Conclusions are presented in Section 6.

2. SPH formalism

The basic principle of the SPH formulation is the integral representation of a function f which may represent a numerical or physical variable defined over a domain of interest Ω at a point $\mathbf{x}$. The integral approximation or kernel approximation reads [6]

$$f(\mathbf{x}) \approx \int_{\Omega} f(\mathbf{x}')W\left(\mathbf{x}-\mathbf{x}', h\right) d\mathbf{x}', \tag{2.1}$$

with h defined as the smoothing length that characterises the size of the support domain of the kernel and W the weighting or kernel function. The kernel function is chosen to be a smooth, isotropic and an even function with

compact support (i.e. the finite radius of influence around $\mathbf{x}$). In this paper, the fifth-order quintic spline kernel with compact support of $3h$ has been used [7]:

$$W(\mathbf{x}-\mathbf{x}',h)=a_d\begin{cases}(3-R)^5-6(2-R)^5+15(1-R)^5, & 0\le R<1;\\ (3-R)^5-6(2-R)^5, & 1\le R<2;\\ (3-R)^5, & 2\le R<3;\\ 0, & R\ge 3;\end{cases}, \tag{2.2}$$

where $R=|\mathbf{x}-\mathbf{x}'|/h$ and the normalisation constant a_d is $7/478\pi$ in 2-D space. High-order kernels will also be used such as the sixth-order Gaussian kernel following Lind and Stansby [5]. The choice of kernels in this work is influenced by the desired accuracy of the interpolation. The fifth-order quintic spline kernel provides a high degree of continuity over a compact domain (helping to minimise discretisation error), while also offering consistency and direct comparison with previous ISPH works [1,2,8]. Meanwhile, the sixth-order Gaussian kernel is necessary to achieve higher-order convergence in Eulerian SPH [5].

In a discrete domain Eq. (2.1) can be approximated by using an SPH summation in the form of

$$\langle f(\mathbf{x})\rangle=\sum_j^N f(\mathbf{x}_j)W(\mathbf{x}-\mathbf{x}_j,h)V_j, \tag{2.3}$$

where V is the volume of the particle expressed as the ratio of the mass m to density ρ and N is the number of particles within the support. Throughout this paper the subscript i denotes the interpolating particle and j refers to the neighbouring particles. The $\langle\cdots\rangle$ symbol denotes an SPH interpolation and will be dropped for simplicity in the rest of the paper. The final form of the particle approximation in a discrete form is

$$f(\mathbf{x}_i)=\sum_j^N \frac{m_j}{\rho_j}f_j W_{ij}, \tag{2.4}$$

with $W_{ij}=W(\mathbf{x}_i-\mathbf{x}_j,h)$ and $f_j=f(\mathbf{x}_j)$. More details of the SPH formulation can be found in [6] and more recently [9].

3. Formulation of the Lagrangian ISPH model

The Navier–Stokes equations in Lagrangian form for an incompressible flow read

$$\nabla\cdot\mathbf{u}=0, \tag{3.1}$$

$$\frac{d\mathbf{u}}{dt}=\frac{1}{\rho}\nabla P+\nu\nabla^2\mathbf{u}+\mathbf{g}, \tag{3.2}$$

where the velocity, pressure, kinematic viscosity, gravity and time are denoted respectively as $\mathbf{u}$, P, ν, $\mathbf{g}$ and t. Herein, incompressibility is enforced in the projection method by a pressure Poisson equation [10]. The discretisation operator for the pressure and viscous terms follows in Section 3.1.

3.1. Discrete SPH operators for the Navier–Stokes equations

The SPH operators employed in this work are similar to [8] and are as follows.

3.1.1. Gradient operator

We employ the following form of the gradient operator

$$\nabla\phi_i=-\sum_j^n V_j\left(\phi_i-\phi_j\right)\nabla W_{ij}, \tag{3.3}$$

where ϕ is a general variable. Lind et al. [11] demonstrated that this form of SPH gradient is best suited for the calculation of the pressure term and therefore is preferred over others. A similar expression is obtained for the divergence operator by decomposing the operator onto a series of gradient operators.

3.1.2. The Laplacian operator

The Laplacian operator employed for a quantity $\mathbf{b}$ is that suggested by Morris et al. [7] and will be referred to as Morris operator henceforth

$$(\nabla \cdot a\nabla \mathbf{b})_i = \sum_j^n \frac{m_j \left(a_i + a_j\right) \mathbf{x}_{ij} \cdot \nabla W_{ij}}{\rho_j (r_{ij}^2 + \eta^2)} \mathbf{b}_{ij}, \tag{3.4}$$

where $\eta = 0.001h$ to avoid singularity as $r_{ij} \to 0$ and r_{ij} is the Euclidian distance. Here, a is a scalar variable. The Laplacian operator was chosen with computational efficiency in mind over other forms such as the Schwaiger operator [12] which improves accuracy near free surfaces and truncated kernel regions [1].

Hence, the Morris operator will be employed only for internal flows. In cases with free-surface flows, the Schwaiger operator is used to provide accurate interpolation near the free surface. The Schwaiger operator reads

$$(\nabla \cdot a\nabla \mathbf{b})_i = \frac{tr\left(\Gamma^{-1}\right)}{n} \left[\begin{array}{l} \displaystyle\sum_j^n \frac{m_j \left(a_i + a_j\right) \mathbf{x}_{ij} \cdot \nabla W_{ij}}{\rho_j (r_{ij}^2 + \eta^2)} \mathbf{b}_{ij} - \\ \qquad (\nabla a_i \mathbf{b}_i - \mathbf{b}_i \nabla a_i + a_i \nabla \mathbf{b}_i) \cdot \displaystyle\sum_j^n \frac{m_j \nabla W_{ij}}{\rho_j} \end{array} \right], \tag{3.5}$$

where Γ is defined as

$$\Gamma^{\alpha\beta} = \sum_j^n \frac{m_j \mathbf{x}_{ij} \cdot \nabla W_{ij}}{\rho_j} \Delta x^\alpha \Delta x^\beta, \tag{3.6}$$

where superscripts α and β denote the spatial coordinates. More details on the performance of the operator can be found in Lind et al. [1] and Schwaiger [12]. It should be noted that both Laplacian operators are non-conservative [1]. The accuracy of this operator has been assessed in Alshaer et al. [13].

3.1.3. Kernel gradient correction

To improve the accuracy near kernel truncated regions and spatially inhomogeneous particle distributions and restore theoretical zero*th* and first order consistency [14] the kernel first derivative is corrected as follows

$$\nabla \widetilde{W}_{ij} = \mathbf{L}(\mathbf{x}) \nabla W_{ij}, \tag{3.7}$$

where

$$\mathbf{L}(\mathbf{x}) = \left[\begin{array}{ll} \displaystyle\sum_j^n V_j x_{ji} \nabla_x W_{ij} & \displaystyle\sum_j^n V_j x_{ji} \nabla_y W_{ij} \\ \displaystyle\sum_j^n V_j y_{ji} \nabla_x W_{ij} & \displaystyle\sum_j^n V_j y_{ji} \nabla_y W_{ij} \end{array} \right]^{-1}, \tag{3.8}$$

in 2-D. For brevity the ($\tilde{}$) symbol is omitted from the gradient operator notation, with correction always applied unless otherwise stated.

3.2. Lagrangian ISPH algorithm

To enforce incompressibility and ensure a divergence free-velocity field, the projection method of Cummins and Rudman [10] as described by Xu et al. [8] has been used. Note, that incompressibility implies no volumetric variations; hence density and mass are constant.

Firstly particles are advected to an intermediate position $\mathbf{x}^*$ with velocity $\mathbf{u}^n$ using

$$\mathbf{x}_i^* = \mathbf{x}_i^n + \mathbf{u}_i^n \Delta t. \tag{3.9}$$

An intermediate velocity $\mathbf{u}^*$ is calculated at position $\mathbf{x}^*$ based on the viscous forces of the momentum equation

$$\mathbf{u}_i^* = \mathbf{u}_i^n + \nu \nabla^2 \mathbf{u}_i^n \Delta t. \tag{3.10}$$

The pressure at time $n+1$ is obtained by the implicit solution of the Poisson equation which has the following form

$$\nabla \cdot \left(\frac{1}{\rho} \nabla P^{n+1} \right)_i = \frac{1}{\Delta t} \nabla \cdot \mathbf{u}_i^*. \tag{3.11}$$

The discretisation of the left hand side of the Poisson equation (3.11) is performed with either the Morris or Schwaiger operator. Next the velocity at time $n+1$ is obtained by the projection of the intermediate velocity onto divergence-free space such that

$$\mathbf{u}_i^{n+1} = \mathbf{u}_i^* - \left(\frac{1}{\rho} \nabla P_i^{n+1} + \mathbf{g} \right) \Delta t, \tag{3.12}$$

resulting in a divergence-free velocity field. Finally the particles are advected to the $n+1$ position by a central difference scheme

$$\widetilde{\mathbf{x}}_i^{n+1} = \mathbf{x}_i^n + \left(\frac{\mathbf{u}_i^{n+1} + \mathbf{u}_i^n}{2} \right) \Delta t. \tag{3.13}$$

In ISPH particles tend to move along the flow field streamlines potentially causing highly distorted inhomogeneous spatial particle spacing and particle clustering that impacts the accuracy of the SPH interpolation [8]. To ensure stability and accuracy of the simulation, after the advection of the particles to $n+1$, particles are shifted to new positions according to a numerical diffusion based on Fick's Law [1], thus the final position of the particles is

$$\mathbf{x}_i^{n+1} = \widetilde{\mathbf{x}}_i^{n+1} + \delta \mathbf{x}_i, \tag{3.14}$$

where $\delta \mathbf{x}_i$ is the shifting distance. Further details of the shifting algorithm used in the ELI-SPH formulation are given in Section 4.3.

The Lagrangian formulation described herein results in a stable algorithm with a near isotropic particle distribution. Although convergence is second order theoretically, numerical experiments in ISPH have shown that the practical order of convergence is close to 1.3 [1]. Indeed as shown by Quinlan et al.[15] the advection of particles in a Lagrangian sense introduces a first-order discretisation error dependent on particle non-uniformity that disrupts second-order convergence. Theoretical convergence can be recovered however, and recently Lind and Stansby [5], demonstrated near ideal convergence in ISPH by using a regular particle distribution (thereby effectively removing error due to non-uniformity) with second and high-order Gaussian kernels.

4. A new Eulerian–Lagrangian ISPH model

4.1. Eulerian ISPH algorithm

In the Eulerian formulation the advection term is retained and the Navier–Stokes equation now reads

$$\frac{\partial \mathbf{u}}{\partial t} + (\mathbf{u} \cdot \nabla)\, \mathbf{u} = -\frac{1}{\rho} \nabla P + \nu \nabla^2 \mathbf{u} + \mathbf{f}. \tag{4.1}$$

As in [5] the particles are fixed in space and the advection term is calculated using an SPH approximation

$$((\mathbf{u} \cdot \nabla)\, \mathbf{u})_i = \sum_j^n V_j \mathbf{u}_{ij} \cdot \left(\mathbf{u}_{ij} \otimes \nabla W_{ij} \right). \tag{4.2}$$

Within the Eulerian formulation, Eqs. (3.9), (3.13) and (3.14) are omitted since particles remain fixed in space. The intermediate velocity calculation of Eq. (3.10) includes the advection term

$$\mathbf{u}_i^* = \mathbf{u}_i^n + \left(\nu \nabla^2 \mathbf{u}_i^n - \left(\mathbf{u}_i^n \cdot \nabla \right) \mathbf{u}_i^n \right) \Delta t, \tag{4.3}$$

with a divergence free velocity field obtained through Eq. (3.12).

Note, that since the Eulerian particle arrangement has a regular (uniform) distribution, the smoothing error is of $O(h^2)$ for spline kernels as demonstrated by Noutcheuwa and Owens [16]. Another clear advantage from a computational point of view is the calculation of the kernel derivatives and neighbour particles can be computed on the first time step and stored unchanged throughout the simulation without the need of kernel correction. A more

detailed description of the Eulerian ISPH formulation can be found in Lind and Stansby [5] and Noutcheuwa and Owens [16].

However, the clear advantage of SPH with its Lagrangian nature capable of simulating highly non-linear problems, such as free surface and interfacial flows, has vanished. To recover the advantages of a Lagrangian method, the coupling of Eulerian–Lagrangian formulations is proposed.

4.2. Eulerian–Lagrangian ISPH algorithm

We wish to maintain the Eulerian formulation at regions away from free surfaces and non-linear interfaces and preserve the $O(h^2)$ convergence characteristics while retaining the Lagrangian formulation of SPH elsewhere. Consequently, an interface can be created allowing controlled introduction of the advection term. In the Eulerian region the advection term is calculated in similar manner to Lind and Stansby [5] and in the Lagrangian region the advection term is absorbed in the velocity derivative yielding a Lagrangian formulation. This is achieved by writing the Navier–Stokes equation in the following form

$$\frac{\partial \mathbf{u}}{\partial t} + (1-\alpha)\,(\mathbf{u}\cdot\nabla)\,\mathbf{u} = -\frac{1}{\rho}\nabla P + \nu\nabla^2\mathbf{u} + \mathbf{f}, \tag{4.4}$$

where the parameter α is 0 or 1 such that

$$\alpha = \begin{cases} 0 & \text{Eulerian} \\ 1 & \text{Lagrangian.} \end{cases} \tag{4.5}$$

Now, Eq. (3.9) reads

$$\mathbf{x}_i^* = \mathbf{x}_i^n + (1-\alpha_i)\,\mathbf{u}_i^n\,\Delta t, \tag{4.6}$$

and Eq. (4.3) retains the advection term so that

$$\mathbf{u}_i^* = \mathbf{u}_i^n + \left(\nu\nabla^2\mathbf{u}_i^n - (1-\alpha_i)\left(\mathbf{u}_i^n\cdot\nabla\right)\mathbf{u}_i^n\right)\Delta t. \tag{4.7}$$

Also, the $n+1$ position of the particles in now obtained by

$$\mathbf{x}_i^{n+1} = \mathbf{x}_i^n + \alpha_i\left(\frac{\mathbf{u}_i^{n+1}+\mathbf{u}_i^n}{2}\right)\Delta t. \tag{4.8}$$

Fig. 4.1 shows a schematic of the proposed configuration, where the two regions are defined.

4.3. Particle shifting for the ELI-SPH

Particle shifting is essential to the creation of a smooth distribution at a sharp interface since a Lagrangian particle would otherwise either move away or towards the Eulerian region resulting in areas of large particle anisotropy. The particle shifting distance $\delta\mathbf{x}_\mathrm{i}$ is governed by Fick's law [1]

$$\delta\mathbf{x}_i = -D_i\nabla\mathbf{C}_i, \tag{4.9}$$

where D is the shifting coefficient and $\nabla\mathbf{C}_i$ is the gradient of particle concentration which is simply the derivative of the kernel zero*th* moment. Herein, a combination of the shifting coefficient of Lind et al. [1] and Skillen et al. [2] has been used to ensure efficient shifting near the interface. The shifting coefficient D reads

$$D_i = \max\left(A_1h^2,\, A_2h|\mathbf{u}|_i\,\Delta t\right), \tag{4.10}$$

where A_1 and A_2 are dimensionless free parameters set to 0.5 and 4 respectively according to Lind et al. [1] and Skillen et al. [2] and additional numerical experiments. Primitive variables such as the field velocity are corrected via a Taylor series expansion for the new shifted position by

$$\phi^{n+1} = \widetilde{\phi}_i^{n+1} + \delta\mathbf{x}_{ii}\cdot\nabla\widetilde{\phi}_i^{n+1} + \mathrm{O}(\delta x_{ii}^2) \tag{4.11}$$

where ϕ is field variable. Note this is a purely numerical device separate from the flow physics.

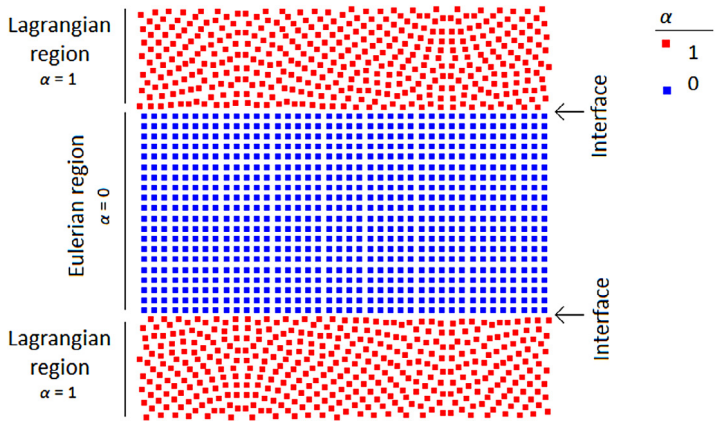

Fig. 4.1. The variation of α at the Eulerian, Lagrangian region and along the interface.

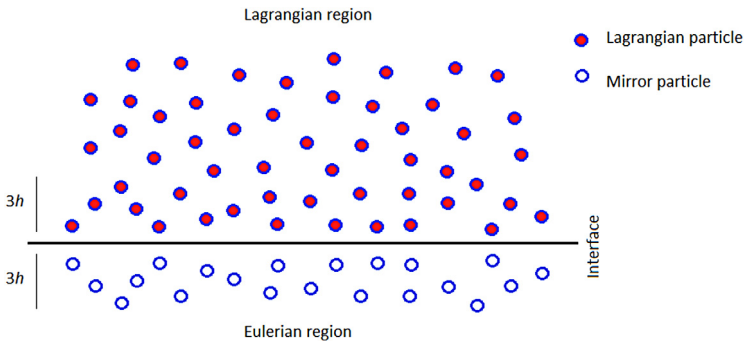

Fig. 4.2. Mirroring of Lagrangian particles at the interface to the Eulerian region.

Near the interface in the Lagrangian region particles are shifted to their new position with the interface treated as a solid boundary. This is achieved by ignoring inner Eulerian particles and by employing the mirroring technique of Morris et al. [7] in order to obtain the concentration gradient at the interface, as shown in the schematic of Fig. 4.2. The Lagrangian region support is thus complete at the interface and truncation is avoided for the concentration gradient in the shifting procedure.

The advantage of the proposed formulation derives from its simplicity and gains in accuracy (see Section 5.1). At the interface there are no overlapping regions and no extra SPH interpolations. The transition between Eulerian and Lagrangian regions occurs without numerical noise, as demonstrated in the next section. The zero divergence condition and hence continuity in mass flux is maintained across the interface.

5. Results and discussion

In this section unbounded, bounded and free-surface flow test cases are presented. The test cases use periodic and wall-bounded flows to demonstrate the effectiveness and improvement in accuracy of the method. Also, free-surface flow test cases have been simulated with success. In addition, higher order kernels have been used in some cases as a proof of concept of efficient and accurate simulation via the particle method equivalent of 'p-adaptivity' [17].

5.1. Taylor–Green vortices

The problem consists of an unbounded periodic 2-D domain of fluid with dimensions of 1 m $\times$ 1 m. The domain is initialised by a smoothed distribution of counter rotating vortices. The flow is incompressible and viscous resulting

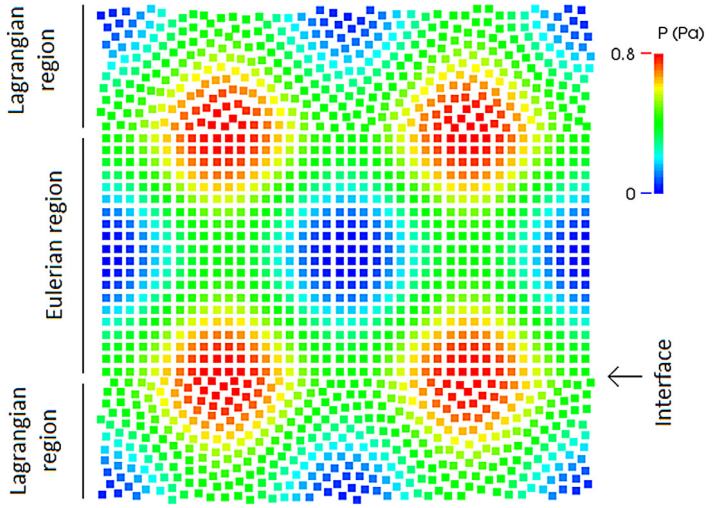

Fig. 5.1. Pressure field of the domain at $t = 1$ s, $Re = 1000$, particle spacing $L/\mathrm{d}x = 40$. Regular distributed particles are Eulerian.

in decaying vortices. The analytical solution for the velocity and pressure field reads

$$\begin{aligned} u &= -e^{f} \cos(2\pi\, x) \sin(2\pi\, y)\,, \\ v &= e^{f} \sin(2\pi\, x) \cos(2\pi\, y)\,, \\ p &= -e^{2f} \left(\cos(4\pi\, x) + \cos(4\pi\, y)\right), \end{aligned} \tag{5.1}$$

where $f = -8\pi^2 t/Re$ and $Re = LU_{max}/\nu$ based on the characteristic length L defined as the vertical length of the square domain with the origin defined at the centre of the domain and U_{max} defined as the maximum velocity of the system. The test case is ideal for assessing the Eulerian–Lagrangian interface since particles stretch and contract creating undesirable particle structures that follow the streamlines of the flow [8].

5.1.1. Eulerian–Lagrangian flow

The Eulerian zone is located within the limits of $y = \pm 0.25$ m with two Lagrangian interfaces at the top and bottom of the Eulerian region.

Fig. 5.1 shows the pressure and particle distribution of the Taylor–Green vortices at $t = 1$ s with a $Re = 1000$ for $L/\mathrm{d}x = 40$ where $\mathrm{d}x$ is the initial particle spacing. The effectiveness of the algorithm is apparent throughout the Lagrangian domain and especially near the interface where voids or high concentration areas are absent with a near regular particle distribution.

Figs. 5.2–5.3 demonstrate the noise-free results obtained for velocity components and pressure of the scheme by comparing the SPH simulation with the analytical solution for the particle resolution of $\mathrm{d}x = 0.0125$ m at $t = 1$ s. The analytical solution is well reproduced for the horizontal and vertical velocity and pressure, without unphysical artefacts near or at the interface. Note, D is the horizontal size of the domain.

To assess the accuracy and numerical convergence, the L_2 error norm in the horizontal velocity over time is computed for the different formulations and three different particle resolutions according to Eq. (5.2). Fig. 5.4 shows a comparison of the ELI-SPH, fully Lagrangian ($\alpha = 1$), and fully Eulerian ($\alpha = 0$) simulations for the particle resolution of $L/\mathrm{d}x = 40$ at $Re = 1000$. Fig. 5.5 shows a comparison of the ELI-SPH and fully Lagrangian ($\alpha = 1$) simulations for three particle resolutions ($L/\mathrm{d}x = 40$, 80, 160) at $Re = 1000$. The reduction in error is clear when the ELI-SPH is employed in comparison to the fully Lagrangian simulation.

$$L_2(u) = \left(\frac{\sum_i \left(u_{i,\text{analytical}} - u_{i,ISPH}\right)^2}{\sum_i u^2_{i,\text{analytical}}} \right)^{\frac{1}{2}}. \tag{5.2}$$

The error remains small over long simulation times as particle resolution increases. More specifically, the error is reduced by 36%, 14.4% and 1.4% respectively for the three particle resolutions. These results demonstrate the

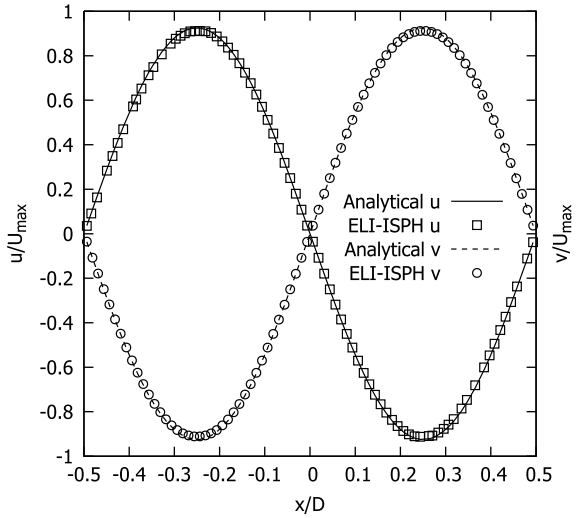

Fig. 5.2. Normalised horizontal and vertical velocity profile along $y/D = 0$ and $x/D = 0$ respectively at $t = 1$ s with $Re = 1000$ and particle resolution $L/\mathrm{d}x = 80$.

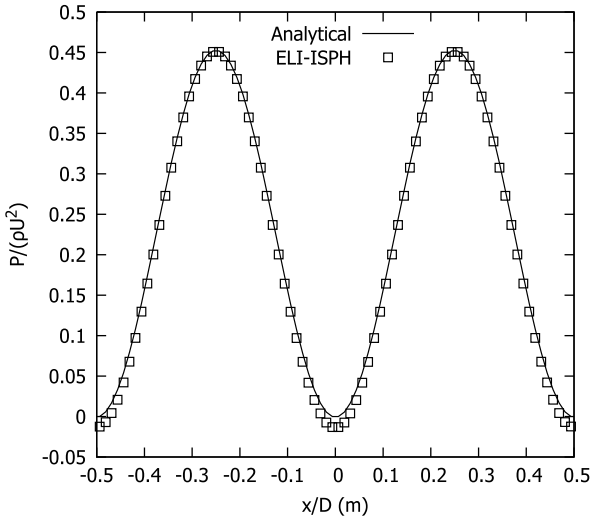

Fig. 5.3. Normalised pressure profile along $y/D = 0$ at $t = 1$ s with $Re = 1000$ and particle resolution $L/\mathrm{d}x = 80$.

advantage of the Eulerian–Lagrangian formulation, as the error in the Eulerian region is significantly lower at the coarser particle resolution of $\mathrm{d}x = 0.025$, as demonstrated in Fig. 5.4. Similar behaviour was observed for longer durations of the simulation.

Fig. 5.6 shows the absolute error in the u velocity at two different time instances, at $t = 1$ s and $t = 5$ s. In Fig. 5.6(a) the error is mainly present in the Lagrangian region, but at $t = 5$ s, the error has appeared in the Eulerian region. Hence, Fig. 5.6 clearly shows that the error propagates from the Lagrangian (non-regular distributed region of particles) to the Eulerian region. Therefore the order of convergence of the domain is dominated by the Lagrangian region.

This is supported by Fig. 5.7 which shows the convergence in $L_2(u)$ error at $t = 1$ s for the $Re = 1000$ case. Although the convergence order remains similar between the purely Lagrangian and ELI-SPH formulation the error reduction for ELI-SPH is apparent. Nevertheless, the order of convergence is lower than the theoretical second order error that is obtained using the Eulerian only formulation as demonstrated by Lind and Stansby [5] due to ELI-SPH error being contaminated by the purely Lagrangian region.

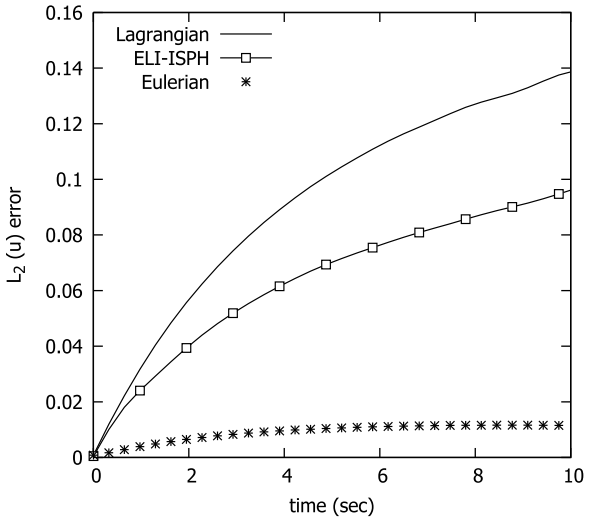

Fig. 5.4. Temporal evolution of L_2 error velocity profile for $L/\mathrm{d}x = 40$ at $Re = 1000$ for all three methods, the purely Lagrangian, ELI-SPH and purely Eulerian formulation.

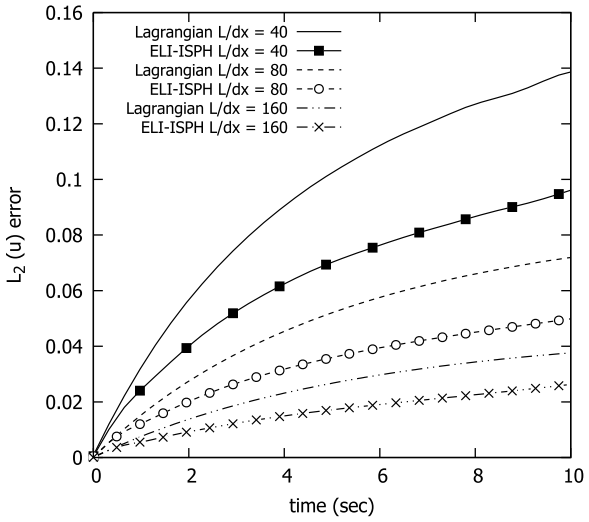

Fig. 5.5. Temporal evolution of L_2 error velocity profile for, $L/\mathrm{d}x = 40$, $L/\mathrm{d}x = 80$ and $L/\mathrm{d}x = 160$ at $Re = 1000$ for the purely Lagrangian and ELI-SPH.

5.1.2. Eulerian–Lagrangian SPH with higher order kernels

Herein, we take advantage of the high order (HO) kernels [5] to improve the error within the Eulerian region.

In the inner Eulerian region (coloured red in Fig. 5.8) the sixth-order Gaussian kernel has been used with a support of $6h$. The support for the high order Gaussian extends only over the uniform spaced particles (i.e. the whole Eulerian region) since the kernel is negative in parts and therefore not suitable for non-uniform (Lagrangian) particle distributions. The Lagrangian region and the outer Eulerian region (both depicted by the blue particles in Fig. 5.8) employ the quintic kernel with $3h$ support. In short, an inner Eulerian particle may only sum over Eulerian particles using the HO kernel whereas, Lagrangian and outer Eulerian particles use the quintic spline kernel.

This three-zone approach avoids kernel mixing and overlapping between the interfaces, as well as the use of specialised multi-kernel SPH formulations.

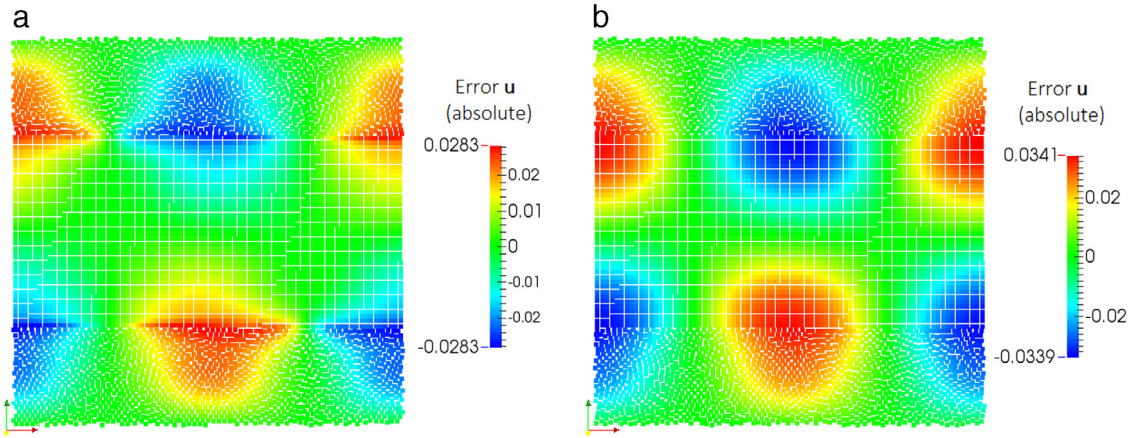

Fig. 5.6. Absolute error in **u** for $L/dx = 80$ and $Re = 1000$ at (a) $t = 1$ s and (b) $t = 5$ s.

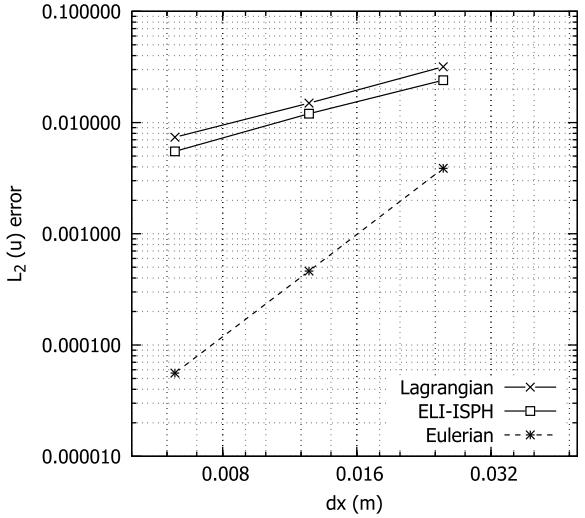

Fig. 5.7. Order of convergence in the error at $t = 1$ s and $Re = 1000$. The solid lines indicate similar order of convergence of approximately 1.25 for the Lagrangian and ELI-ISPH, dotted line indicate an order of approximately 2.85 order of convergence for the purely Eulerian formulation.

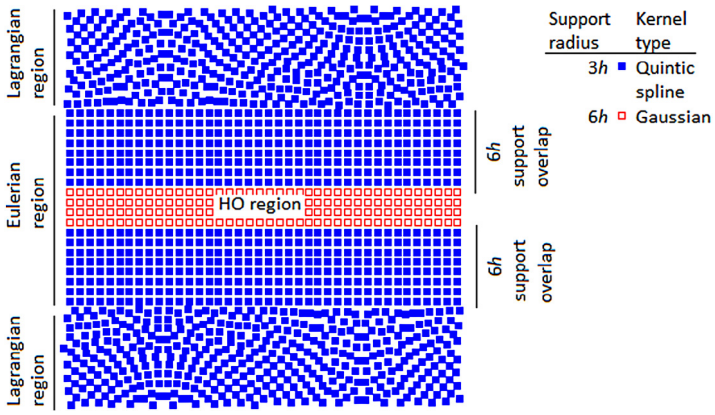

Fig. 5.8. Schematic of the Lagrangian, Eulerian and HO Eulerian regions for the HO kernel configuration.

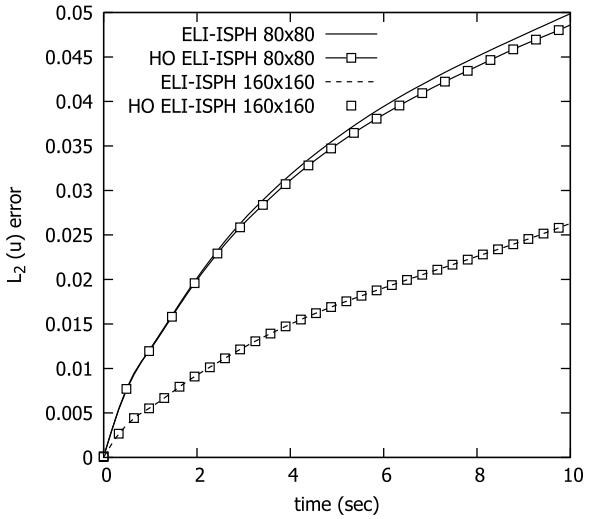

Fig. 5.9. Temporal evolution of L_2 error velocity profile at $Re = 1000$ using high order kernels.

The aim here is to demonstrate a methodology where the high-order Eulerian region retains improved error performance within the Eulerian region. The proposed methodology may be used for a future straightforward p-adaptivity method with improved accuracy in SPH.

Results of the L_2 error from the temporal evolution of the horizontal velocity are shown in Fig. 5.9 illustrating some improvement with high-order kernels at coarser resolution. They extend over a limited zone in the centre of the domain and the high-order kernel support overlaps over most of the quintic Eulerian region where the error is of $O(h^2)$. This error propagates into the high-order region. Clearly, there is benefit in maximising the extent of the high-order region as there also would be in increasing the time integration scheme to second order [5].

This gain in accuracy within the high-order Eulerian region may be exploited within a variable-resolution framework in view of the fact a lower resolution with a high-order kernel may be used to maintain an overall error level consistent with any nearby Lagrangian region. Although this concept is not demonstrated here, investigations into a variable resolution, multi-kernel SPH methodology are underway.

5.2. *Vortex spin-down*

In a similar manner to the Taylor–Green vortices, the domain is initialised by a smooth distribution of a clockwise rotating vortex such that

$$\begin{aligned} u &= U_{\max}(y - 0.5) \\ v &= U_{\max}(0.5 - x)' \end{aligned} \tag{5.3}$$

where $U_{max} = 1$ m/s and refers to the maximum velocity of the system. However, in the vortex spin-down test case the domain is bounded by walls with dimensions of 1 m $\times$ 1 m with the origin located at the left bottom of the domain. As in the previous test case, the flow is incompressible and viscous resulting in a decaying vortex. The vortex spin-down test case demonstrates the ability of the proposed methodology to treat flows where the interface interacts with the walls. Note that the mirroring methodology of Morris et al. [7] is employed to model the wall boundary conditions.

In the absence of an analytical solution, the finite volume software StarCCM+ has been taken as the reference solution using a second order differencing scheme for the advection term with PISO velocity–pressure coupling and a convergence criterion of 10^{-5} using 25 600 cells [8]. Fig. 5.10 shows the pressure at $t = 10$ s as well as the location of the Eulerian and Lagrangian region separated by the interface. Notably, as with the Taylor–Green vortices, the interface shows near isotropic particle distribution without any spurious pressure noise.

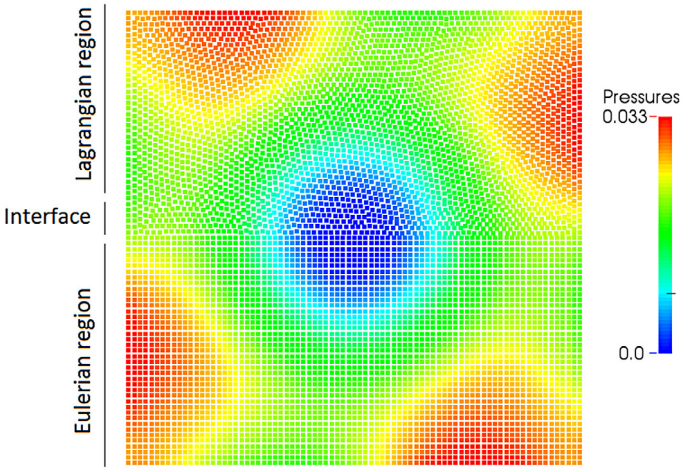

Fig. 5.10. Pressure field of the vortex spin-down case for 80×80 particles with $Re = 1000$ and $t = 10$ s.

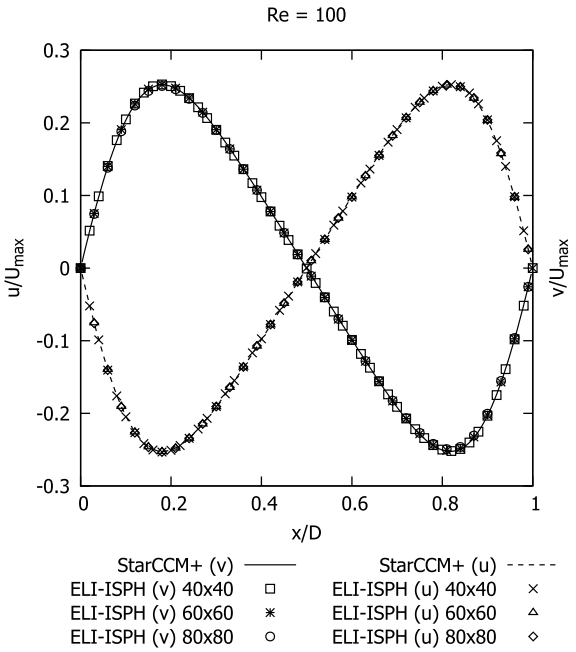

Fig. 5.11. Comparison between StarCCM+ and ELI-SPH for the normalised horizontal and vertical velocity profile along $y/D = 0$ and $x/D = 0$ respectively at $t = 1$ s with $Re = 100$ and for three particle resolutions ($L/\mathrm{d}x = 40$, $L/\mathrm{d}x = 60$ and $L/\mathrm{d}x = 80$).

Figs. 5.11 and 5.13 show a comparison of the velocity results obtained by StarCCM+ and ELI-ISPH for the horizontal and vertical directions for three different resolutions at $Re = 100$ and $Re = 1000$ respectively. Pressure comparison plots are presented in Figs. 5.12 and 5.14 for the aforementioned Reynolds numbers. Note that the interface is located at $y/D = 0.5$. The StarCCM+ solution is well reproduced by ELI-SPH without any spurious fluctuations near or around the interface and the wall solid boundary especially for the challenging horizontal profile which is located at the interface along the whole length of the domain. The pressure field is also well reproduced. Increasing resolution shows the ELI-SPH results converge to the StarCCM+ results.

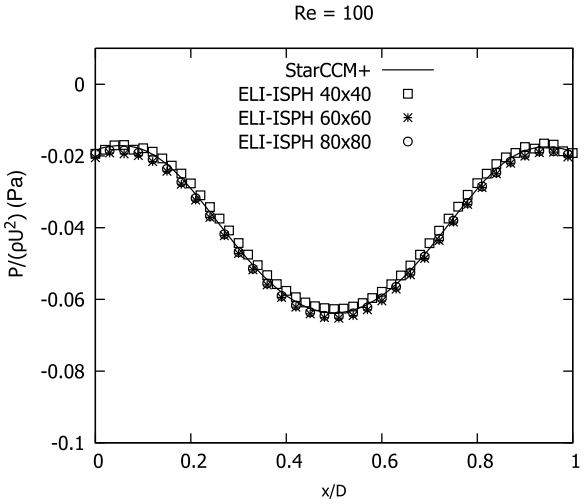

Fig. 5.12. Comparison between StarCCM+ and ELI-SPH for the normalised horizontal pressure profile along $y/D = 0.5$ at $t = 1$ s with $Re = 100$ and for three particle resolutions ($L/\mathrm{d}x = 40$, $L/\mathrm{d}x = 60$ and $L/\mathrm{d}x = 80$).

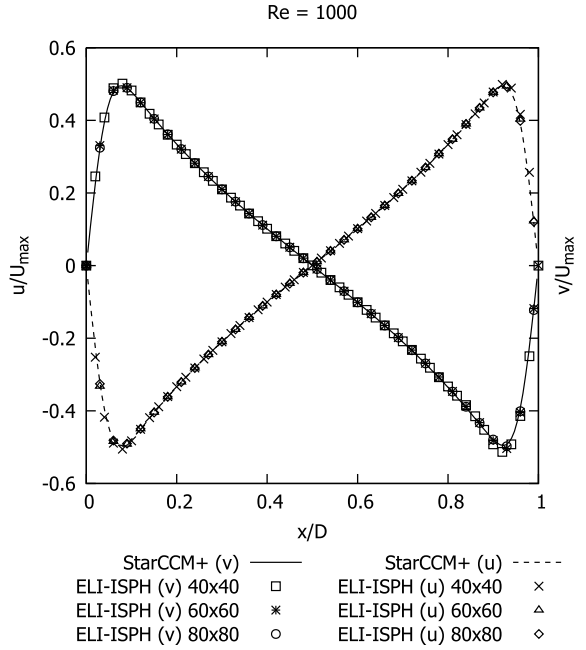

Fig. 5.13. Comparison between StarCCM+ and ELI-SPH for the normalised horizontal and vertical velocity profile along $y/D = 0$ and $x/D = 0$ respectively at $t = 1$ s with $Re = 1000$ and for three particle resolutions ($L/\mathrm{d}x = 40$, $L/\mathrm{d}x = 60$ and $L/\mathrm{d}x = 80$).

5.3. Lagrangian vortex spin-down with Eulerian boundary conditions

An additional benefit of this development is that a simple solid boundary condition may simply be provided within a mostly Lagrangian simulation by imposing layers (usually three) of fixed (Eulerian) particles adjacent to the solid surface within the fluid domain and at mirror positions within the solid surface (or vice versa). Outside the region of the Eulerian fluid particles the fluid particles revert to Lagrangian form. This is relatively easy to set up with the usual care required for sharp corners using mirror particles [2].

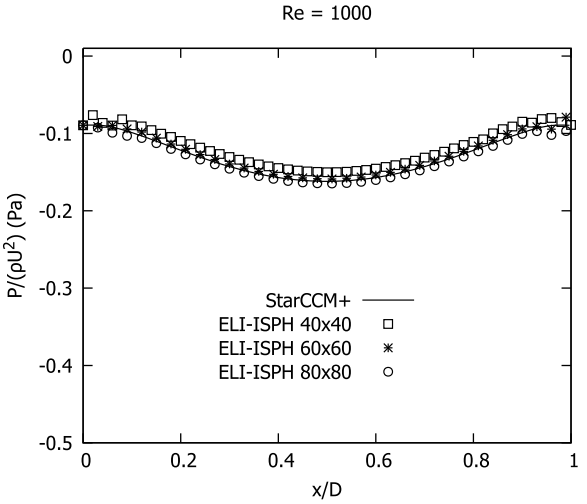

Fig. 5.14. Comparison between Star CCM+ and ELI-SPH for the normalised horizontal pressure profile along $y/D = 0.5$ at $t = 1$ s with $Re = 1000$ and for three particle resolutions ($L/\mathrm{d}x = 40$, $L/\mathrm{d}x = 60$ and $L/\mathrm{d}x = 80$).

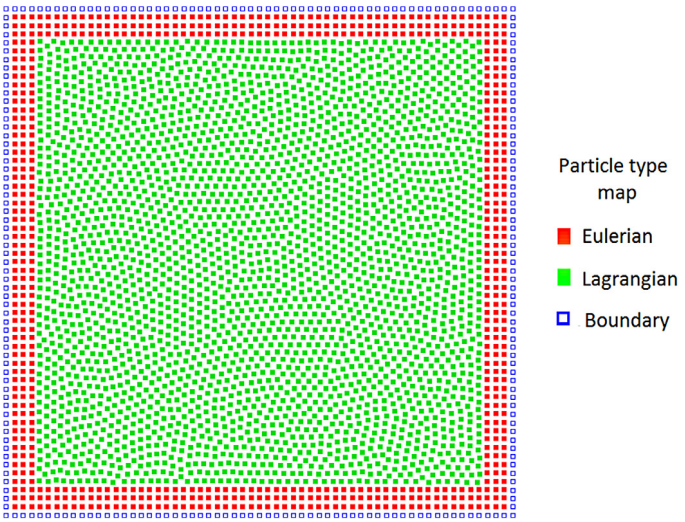

Fig. 5.15. Particle type arrangement for the Eulerian wall boundary condition. Red particles (uniformly distributed) denote Eulerian particles near the wall boundary.

This is conveniently demonstrated here for the vortex spin-down problem. Fig. 5.15 shows the particle arrangement for the vortex spin down case. Three layers of Eulerian particles (i.e. the particles required to fill our $3h$ support) are uniformly distributed near the wall. These particles are purely Eulerian in a similar manner as with the ELI-SPH. However, the Eulerian particles pose an advantage. Mirroring of the particles properties or applying other velocity interpolation such as finite differences or a high order extrapolation becomes trivial in the uniform grid. Herein, we demonstrate the methodology of the Eulerian boundary particle approach, with detailed studies on accuracy and convergence reserved for a future paper.

Comparisons are shown between StarCCM+ and ISPH with the proposed Eulerian boundary condition (ELI-SPH BC) in Fig. 5.16 to Fig. 5.17 for the velocity profile along $y/D = 0.5$ and pressure field at $t = 1$ s, with very good agreement between the ELI-SPH BC and StarCCM+.

Using StarCCM+ as a reference solution, a comparison between the horizontal velocity error (defined as $|u_{\mathrm{SPH}} - u_{\mathrm{starccm+}}|/U_{\max}$ of the Lagrangian and ELI-ISPH BC for the velocity profile near the wall boundary along

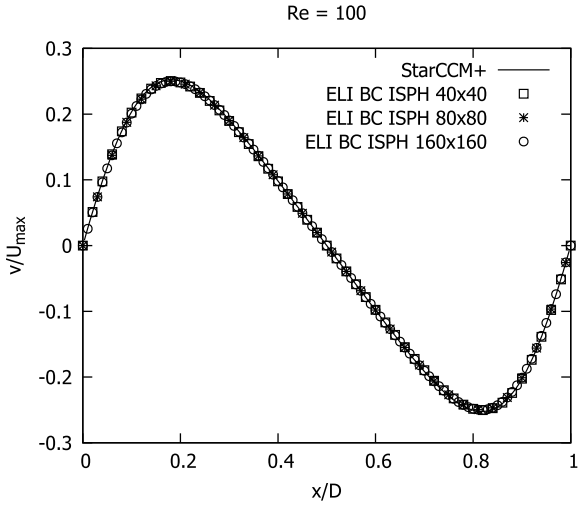

Fig. 5.16. Comparison between StarCCM+ and Eulerian wall boundary for the normalised horizontal velocity and pressure profile along $y/D = 0.5$ at $t = 1$ s with $Re = 100$ and for three particle resolutions ($L/\mathrm{d}x = 40$, $L/\mathrm{d}x = 80$ and $L/\mathrm{d}x = 160$).

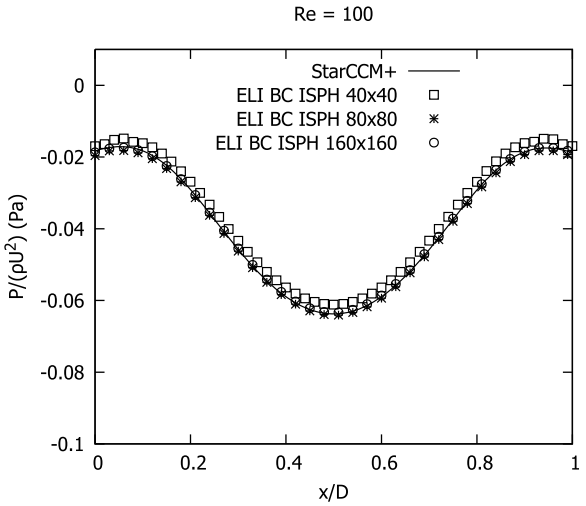

Fig. 5.17. Comparison between StarCCM+ and Eulerian wall boundary for the normalised horizontal pressure profile along $y/D = 0.5$ at $t = 1$ s with $Re = 100$ and for three particle resolutions ($L/\mathrm{d}x = 40$, $L/\mathrm{d}x = 80$ and $L/\mathrm{d}x = 160$).

$y/D = 0.5$ at $t = 1$ s is shown in Fig. 5.18. Clearly, there is a demonstrable improvement in accuracy using the ELI-SPH BC over the purely Lagrangian formulation.

5.4. Periodic wave propagation

Although the previous test cases demonstrated the flexibility and error reduction through the purely Eulerian region with an interface to a purely Lagrangian region in unbounded and bounded test cases, the attractiveness of the ELI-ISPH formulation can be further demonstrated using a simple free-surface flow case, such as a periodic wave propagation. In the presence of a free-surface, a Lagrangian region is present in the area of high non-linearity and a fully Eulerian region is defined near the bed and away from the free-surface. The aim of this test case is to demonstrate the functionality of the ELI-SPH to deal with non-linear free-surface flows.

Herein, we consider a non-linear inviscid progressive gravity wave within a periodic domain of length equal to two wave lengths with a wave length of $\lambda = 3.922$ m and a period of $t = 1.65$. The initial water depth is $d = 1.0$ m

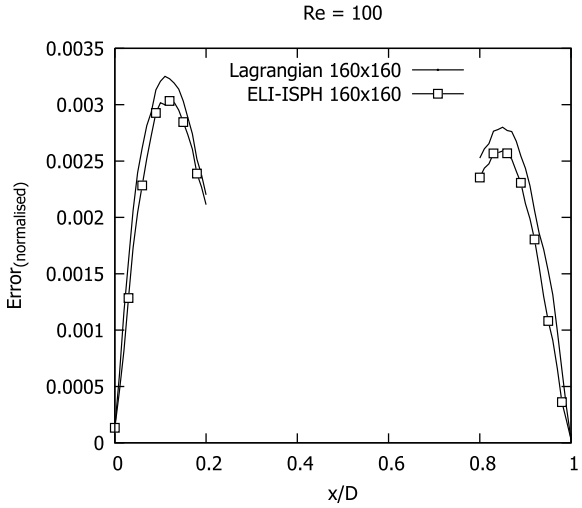

Fig. 5.18. Comparison of the horizontal velocity error profile of the Lagrangian and Eulerian wall boundary along $y/D = 0.5$ at $t = 1$ s with $Re = 100$ for $L/dx = 160$ (reference solution from StarCCM+).

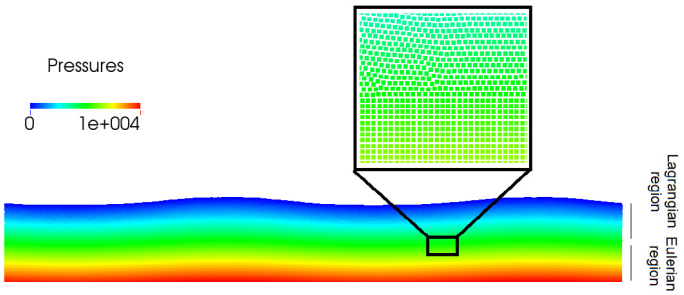

Fig. 5.19. Pressure (Pa) and particle distribution at 10 periods of a wave propagating in the periodic domain and of particle distributions over the Eulerian to Lagrangian region.

and a wave height of $H = 0.12$ m. The velocity field and free-surface location is prescribed by SAWW [18] as initial conditions at time $t = 0.0$ s which is based on the irrotational stream function theory [19].

Fig. 5.19 shows the pressure field of the Eulerian and Lagrangian region after 10 wave periods with the interface defined at $y = 0.5$ m (which is half the water depth) and includes a close-up of the particle distribution at the interface. The resulting Lagrangian particle distribution is near isotropic with an absence of voids or high concentration areas or pressure fluctuations.

Figs. 5.20–5.21 show the normalised peak height and trough height respectively for 10 periods. Three different particle resolutions have been used to demonstrate the convergence characteristics. As shown in Fig. 5.20 the wave decay after 10 periods is close to 0.5%, which is satisfactory and in approximate agreement with Skillen et al. [2]. Fig. 5.22 presents the wave height profile over 10 periods for 3 different resolutions at the location of $x/\lambda = 0.5$. Evidently the resolution of $\lambda/dx = 400$ shows minimal decay. Note that the time integration used in ELI-ISPH is only first order, thus some wave height decay is present, also shown in the normalised kinetic energy of Fig. 5.23. Similar characteristics are observed by [2].

The velocity profile at the peak and trough from the ELI-ISPH is compared with the irrotational stream function theory profiles obtained from SAWW and presented in Fig. 5.24 and Fig. 5.25 for the horizontal and vertical velocity, with good agreement shown. Note, that the interface between the Eulerian and Lagrangian region did not produce any spurious velocity fluctuations.

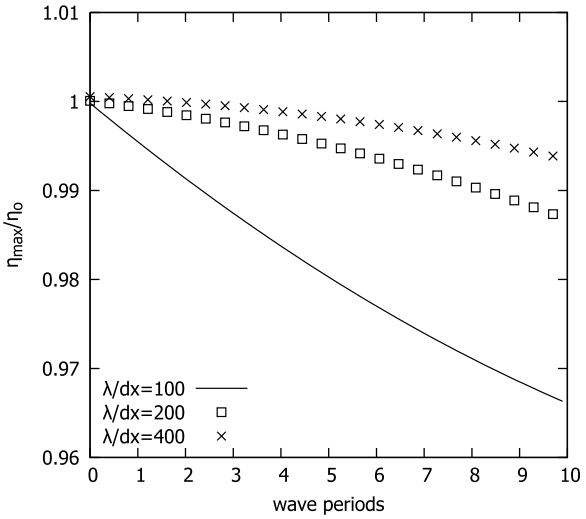

Fig. 5.20. Maximum free-surface elevation (crest) over first 10 periods of a wave propagating in the periodic domain for 3 different particle resolutions using the ELI-SPH formulation.

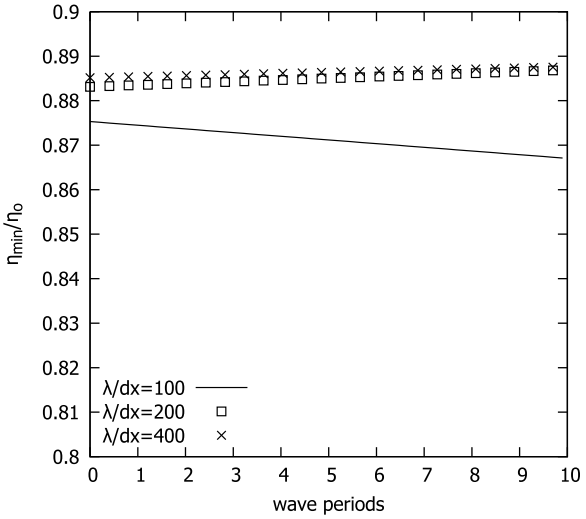

Fig. 5.21. Minimum free-surface elevation (trough) over first 10 periods of a wave propagating in the periodic domain for 3 different particle resolutions using the ELI-SPH formulation.

6. Conclusions and future work

An Eulerian–Lagrangian ISPH formulation is proposed that improves the accuracy of the SPH solution by controlling the particle uniformity. Regions with a free surface (or interfacial flows) remain Lagrangian whereas regions away from such non-linear phenomena are treated using the Eulerian form. Also, for a conventional fully Lagrangian formulation a simple general solid boundary condition is proposed using the Eulerian formulation near wall boundaries.

A number of cases have been presented. The Taylor–Green vortex is an ideal case to assess the accuracy of the proposed methodology. Results have shown that there are potentially significant benefits in error reduction when the ELI-SPH is employed over the Lagrangian form. The wall bounded case of vortex spin-down in a square box has been presented to highlight the flexibility of the proposed scheme and its applicability to internal wall bounded flows. This test case also demonstrates how use of layers (usually three) of fixed fluid particles close to the wall with mirror

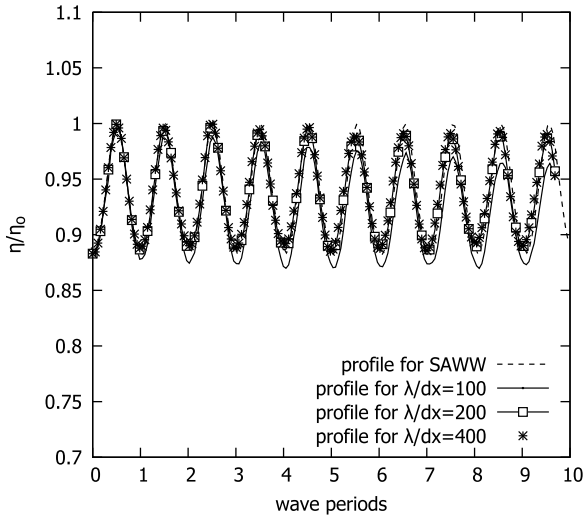

Fig. 5.22. Wave height profile over first 10 periods of a wave propagating in the periodic domain for 3 different particle resolutions using the ELI-SPH formulation and comparison with SAWW at location $x/\lambda = 0.5$.

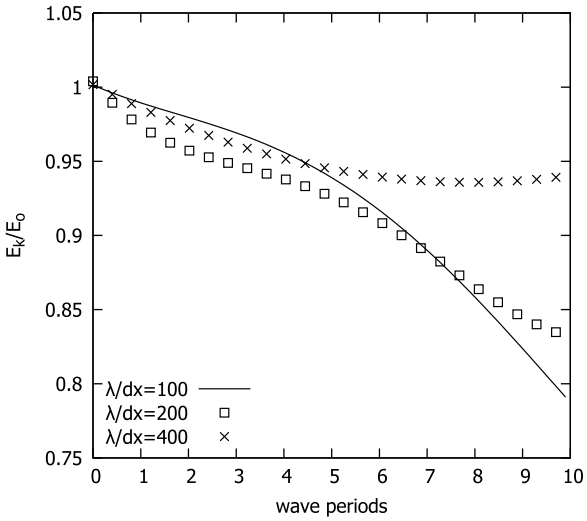

Fig. 5.23. Normalised kinetic energy over first 10 periods of a wave propagating in the periodic domain for 3 different particle resolutions using the ELI-SPH formulation.

particles provides a simple solid boundary representation within an otherwise Lagrangian formulation. The scheme was also applied to free-surface flows using a propagating periodic wave without the need of special treatments at the Eulerian–Lagrangian interface with good agreement to the stream function theory solution of SAWW demonstrated.

In future work, the novel Eulerian–Lagrangian formulation will be extended to an arbitrary Eulerian–Lagrangian scheme which, as mentioned, can be complemented with efficient variable particle resolution and multi-kernel approaches for sustaining accuracy at low resolution. Also, the Eulerian boundary condition approach holds promise in allowing an accurate and straightforward implementation of boundary conditions in SPH, which have long been an issue and a topic of sustained research in the SPH community. Further detailed studies on the accuracy and convergence of the ELI-SPH BC for a range of test cases are reserved for a future paper with the addition of a 3-D implementation.

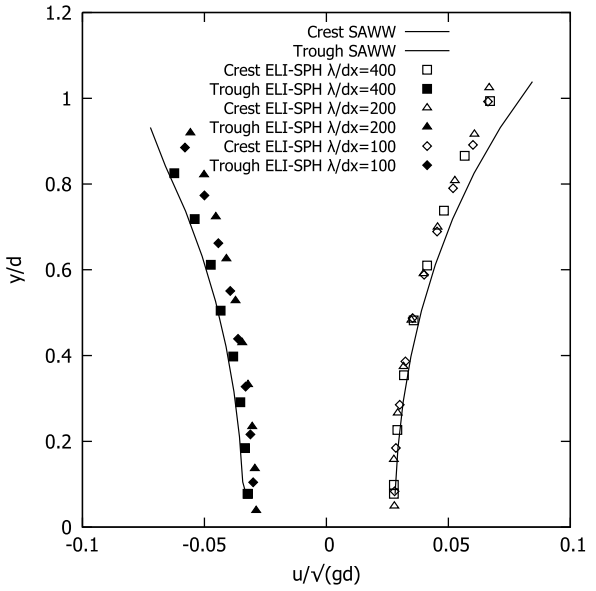

Fig. 5.24. Velocity prediction comparison between ELI-ISPH and SAWW in the horizontal direction over a crest and trough after the first 10 periods of a wave propagating in the periodic domain for 3 different particle resolutions using the ELI-SPH formulation.

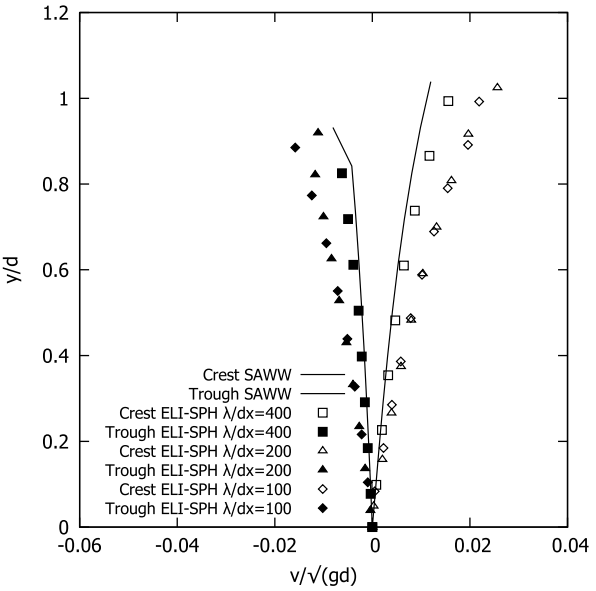

Fig. 5.25. Velocity prediction comparison between ELI-ISPH and SAWW in the vertical direction over a crest and trough after the first 10 periods of a wave propagating in the periodic domain for 3 different particle resolutions using the ELI-SPH formulation.

Acknowledgements

This work has been funded by the EPSRC, UK [grant numbers EP/L014661/1 and EP/L014890/1].

References

[1] S.J. Lind, R. Xu, P.K. Stansby, B.D. Rogers, Incompressible smoothed particle hydrodynamics for free-surface flows: A generalised diffusion-based algorithm for stability and validations for impulsive flows and propagating waves, J. Comput. Phys. 231 (2012) 1499–1523.

[2] A. Skillen, S. Lind, P.K. Stansby, B.D. Rogers, Incompressible smoothed particle hydrodynamics (SPH) with reduced temporal noise and generalised Fickian smoothing applied to body–water slam and efficient wave–body interaction, Comput. Methods Appl. Mech. Engrg. 265 (2013) 163–173.
[3] J. Bonet, T.S.L. Lok, Variational and momentum preservation aspects of Smooth Particle Hydrodynamic formulations, Comput. Methods Appl. Mech. Engrg. 180 (1999) 97–115.
[4] A. Chaniotis, D. Poulikakos, P. Koumoutsakos, Remeshed smoothed particle hydrodynamics for the simulation of viscous and heat conducting flows, J. Comput. Phys. 182 (2002) 67–90.
[5] S.J. Lind, P.K. Stansby, High-order Eulerian incompressible smoothed particle hydrodynamics with transition to Lagrangian free-surface motion, J. Comput. Phys. 326 (2016) 290–311.
[6] R.A. Gingold, J. Monaghan, Smoothed particle hydrodynamics: theory and application to non-spherical stars, Mon. Not. R. Astron. Soc. 181 (1977) 375–389.
[7] J.P. Morris, P.J. Fox, Y. Zhu, Modeling low reynolds number incompressible flows using SPH, J. Comput. Phys. 136 (1997) 214–226.
[8] R. Xu, P. Stansby, D. Laurence, Accuracy and stability in incompressible SPH (ISPH) based on the projection method and a new approach, J. Comput. Phys. 228 (2009) 6703–6725.
[9] D. Violeau, B.D. Rogers, Smoothed particle hydrodynamics (SPH) for free-surface flows: past, present and future, J. Hydraul. Res. 54 (2016) 1–26.
[10] S.J. Cummins, M. Rudman, An SPH projection method, J. Comput. Phys. 152 (1999) 584–607.
[11] S.J. Lind, P.K. Stansby, B.D. Rogers, Incompressible–compressible flows with a transient discontinuous interface using smoothed particle hydrodynamics (SPH), J. Comput. Phys. 309 (2016) 129–147.
[12] H.F. Schwaiger, An implicit corrected SPH formulation for thermal diffusion with linear free surface boundary conditions, Internat. J. Numer. Methods Engrg. 75 (2008) 647–671.
[13] A. Alshaer, B.D. Rogers, L. Li, Smoothed Particle Hydrodynamics (SPH) modelling of transient heat transfer in pulsed laser ablation of Al and associated free-surface problems, Comput. Mater. Sci. 127 (2017) 161–179.
[14] G. Oger, M. Doring, B. Alessandrini, P. Ferrant, An improved SPH method: Towards higher order convergence, J. Comput. Phys. 225 (2007) 1472–1492.
[15] N.J. Quinlan, M. Basa, M. Lastiwka, Truncation error in mesh-free particle methods, Int. J. Numer. Methods Eng. 66 (2006) 2064–2085.
[16] R.K. Noutcheuwa, R.G. Owens, A new incompressible smoothed particle hydrodynamics-immersed boundary method, Int. J. Numer. Anal. Model. 3 (2012) 126–167.
[17] R. Vacondio, B.D. Rogers, P.K. Stansby, P. Mignosa, J. Feldman, Variable resolution for SPH: A dynamic particle coalescing and splitting scheme, Comput. Methods Appl. Mech. Engrg. 256 (2013) 132–148.
[18] G.Y. Buss, P.K. Stansby, SAWW - A Computer Program to Calculate the Properties of Steady Water Waves, Techical Report, Simon Engineering Laboratories, University of Manchester, 1982.
[19] M. Rienecker, J. Fenton, Fourier approximation method for steady water waves, J. Fluid Mech. 104 (1981) 119–137.